ADVANCED MATERIALS TECHNOLOGIES
www.advmattechnol.de

Na-Ion Battery with Graphite Anode and $Na_3V_2(PO_4)_3$ Cathode via Solvent-Co-Intercalation Process

*Krishnan Subramanyan, Manohar Akshay, Yun-Sung Lee, and Vanchiappan Aravindan**

Spent Li-ion batteries are efficiently recycled by extracting and reusing the anode active material, graphite, through a simple yet effective and scalable technique as anode for the sodium-ion battery (SIB). The recovered graphite (RG) half-cell rendered a capacity of >120 mAh g^{-1} via the solvent-co-intercalation process. An in situ impedance is performed to assess the robustness of the electrolyte for the extended cycling. The performance of RG is evaluated in a full-cell with carbon-coated $Na_3V_2(PO_4)_3$ cathode, which exhibits capacity retention of 78% after 100 cycles. In addition, a temperature dependence performance of the full-cell is studied from −10 to 40 °C, where it exhibits outstanding low-temperature performance. The full-cell provides an energy density of 78 Wh kg^{-1} at ambient temperature conditions. Recovery of active materials for SIB will drive down the cost/kWh and act as a green technology to dispose of spent Li-ion batteries.

1. Introduction

Renewable energy sources are efficient and pragmatic to combat energy crunch in the future via a greener, eco-friendly approach by cutting down greenhouse gas emissions. Unfortunately, these sources are intermittent and discontinuous, affecting their feasibility. Using an energy storage device will mitigate this and facilitate load leveling. Thanks to years of research and development, lightweight, high gravimetric and volumetric energy density, and durable performance have made lithium-ion batteries (LIBs) the front-runner in the battery industry.[1] Regardless, the search for alternative battery systems is inevitable due to depleting lithium resources, a complex supply–demand chain, costly transition metals, and political and geographical issues in mining this raw materials.[2–5] These factors have made Na-ion-based energy storage in batteries and capacitors a viable solution for stationary/grid energy storage applications and electric vehicle (EV) batteries. Recycling or proper disposal is the crucial aspect that completes the life of a LIB, and the increasing demand/usage of LIBs calls for a boost in recycling. The anode active material in commercialized LIBs, graphite, was thought to be electrochemically inactive in Na-ion-based energy storage. This is true when carbonate-based electrolytes were used due to the unstable binary graphite intercalation compounds (*b*-GIC) formed with Na.[6] When ether-based electrolytes are introduced, there is a formation of [Na-co-solvent]$^+$, intercalated into the graphitic structure to form a ternary-GIC (*t*-GIC). *t*-GIC was found to remain stable since the [Na-co-solvent]$^+$ LUMO energy levels were above the Fermi level of graphite which did not allow the decomposition of [Na-co-solvent]$^+$[7–11]. Co-intercalation has been explored for Li, K, and even multication solvent co-intercalation.[12]

In this line, our work aims to reuse graphite recovered from spent LIBs as an anode in a sodium-ion battery (SIB) with a co-intercalation-based mechanism. Our group has explored recycling graphite from spent LIBs, which was used in LIBs,[13] Li-ion capacitors,[14,15] and even Na-ion capacitors.[16] The recycling method is efficiently used, succeeded by pyrolysis to recover graphite, and used as anode in a SIB in both half-cell and full-cell configuration by pairing with a carbon-coated $Na_3V_2(PO_4)_3$ cathode (NVPC). A similar attempt to recycle graphite through an acid-assisted method has been reported and electrochemically tested in a half-cell. However, its performance in a full-cell has not been evaluated.[17] The novelty of this work is that we first attempted to explore the performance of a Na-ion full-cell constructed with graphite recovered directly from a discarded LIB without any further treatment. The half-cell exhibited excellent initial Coulombic efficiency (>87%), capacity retention of 84% after 100 cycles at a current density of 50 mA g^{-1}, with a minimal loss of 10% capacity. A temperature study with temperatures ranging from −10 to 40 °C showed the excellent capacity retention of the cell and described it in detail.

2. Results and Discussion

The X-ray diffraction (XRD) pattern of recovered graphite (RG) is shown in **Figure 1**a. The pattern shows the characteristic sharp peak of graphite at 26.5°, and all the other peaks match exactly with graphite's XRD peaks (DB card no. 03-065-6212) belonging to the space group $P6_3/mmc$. The unit cell parameters are $a = b = 2.4621$ Å, and $c = 6.7177$ Å, $\alpha = 90°$, $\beta = 90°$, and

K. Subramanyan, M. Akshay, V. Aravindan
Department of Chemistry
Indian Institute of Science Education and Research (IISER) Tirupati
Tirupati 517507, India
E-mail: aravindan@iisertirupati.ac.in
Y.-S. Lee
School of Chemical Engineering
Chonnam National University
Gwang-ju 61186, Republic of Korea

The ORCID identification number(s) for the author(s) of this article can be found under https://doi.org/10.1002/admt.202200399.

DOI: 10.1002/admt.202200399

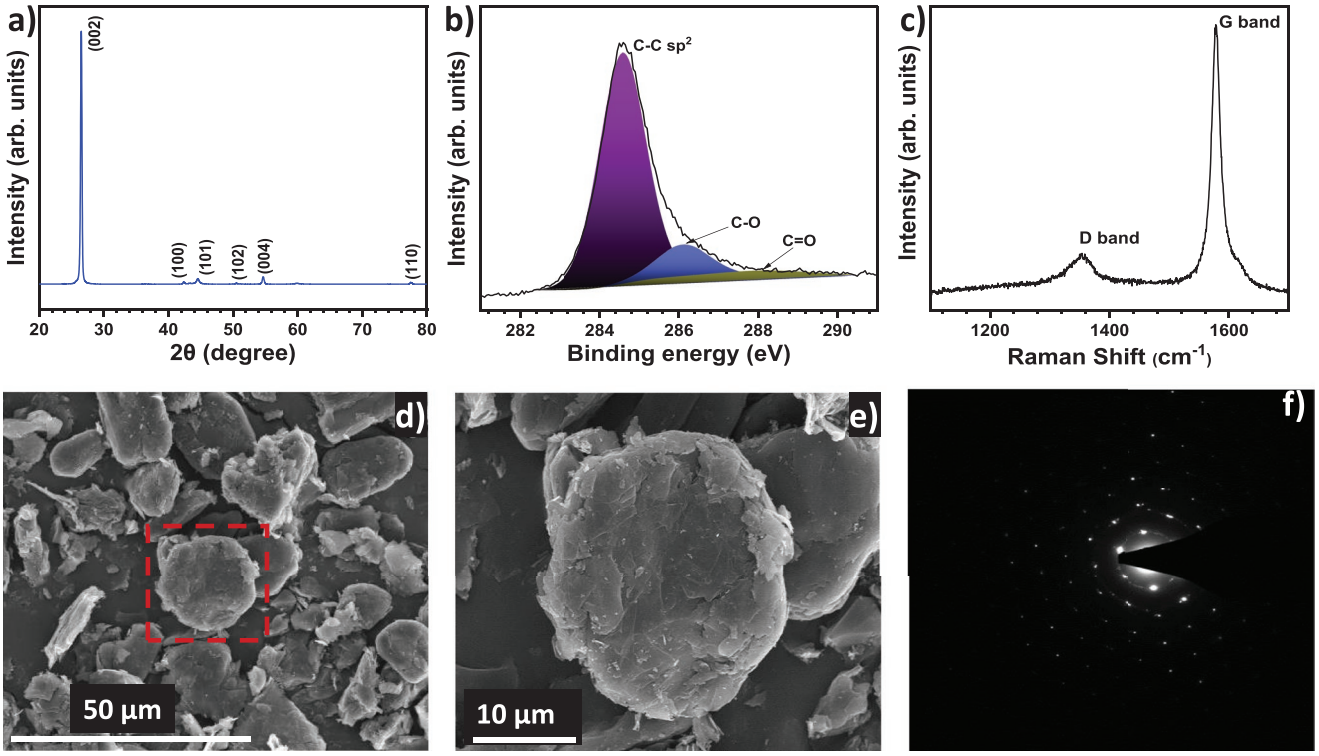

Figure 1. a) Powder XRD, b) high-resolution XPS spectra for carbon (C1s), c) Raman spectra, d,e) FE-SEM images, and f) SAED pattern of RG.

$\gamma = 120°$ (unit cell volume = 40.72 Å^3). The absence of any additional peaks indicates the purity, and sharp peaks mark RG's highly crystalline nature. Based on the peak at 26.5°, which corresponds to the *hkl* plane (002), the separation between two graphene layers is 0.336 Å. We calculated the RG particle size using the Debye–Scherrer equation for the (002) peak

$$D = \frac{0.9\lambda}{\beta \cos\theta} \quad (1)$$

where λ is the wavelength of the X-ray source used, β is the full width at half maximum of the peak in radians, and θ is the Braggs angle in radians. The particle size was found to be ≈34 nm.

A high-resolution X-ray photoelectron spectroscopy (XPS) study of RG reveals the presence of carbon and oxygen indicated by the C 1s and O 1s peaks (Figure S1, Supporting Information). The minor O 1s may imply the presence of graphene oxide in the sample. The minimal amount of the graphene oxide present is confirmed when the C 1s peak is deconvoluted (Figure 1b), where the strongest signal arises from the C—C sp^2 bond (284.6 eV) followed by C—O (286.1 eV) and C=O (287.6 eV) bonds.[18] The presence of an ordered structure is further demonstrated in the Raman spectra of RG with I_D/I_G = 0.20. The particle morphology, size, and composition of RG were studied with imaging techniques like field emission scanning electron microscopy (FESEM) and high-resolution tunneling electron microscopy (HRTEM). The SEM image (Figure 1d,e) shows flakes of graphite and agglomerations of graphite which are a few tens of micrometers in size. The elemental analysis (Figure S2a, Supporting Information) shows only the presence of carbon, ensuring no impurities and the oxygen content is negligible. The HRTEM image (Figure S2b, Supporting Information) reveals regularly spaced lattice planes, and the selected area electron diffraction (SAED) pattern with highly defined rings indicates graphite's highly ordered and crystalline nature. The characterization techniques suggest that after many cycles in LIBs, the graphite can be recovered through our technique while preserving its structure and crystallinity.

2.1. Half-Cell Performance

The electrochemical performance of RG was assessed through a Na/RG half-cell. Cyclic voltammetry of the cell was done at various scan rates from 0.005 to 2.50 V (**Figure 2**a). In the case of the cathodic scan at 0.1 mV s^{-1} (OCV: 0.005 V vs Na), there is one prominent sharp peak at ≈0.72 V vs Na and one minor sharp peak positioned at ≈0.45 V vs Na. The current value for these peaks increases with scan rate and is observed to shift to lower potential as scan rate changes from 0.1 to 1 mV s^{-1} and eventually merges. There are multiple small peaks at 0.006, 0.83, 0.93, and 1.06 V vs Na when the scan rate is at 0.1 mV s^{-1}. Apart from the peak at 0.006 V vs Na, the other peaks merge at higher scan rates to form a broad peak. These correspond to the formation of the *t*-GIC phase, where sodium is stored in graphite through co-intercalation. At 0.1 mV s^{-1}, two sharp and distinct peaks are visible at 0.49 and 0.83 V vs Na during the anodic scan. Besides, a small broad peak located at 1.21 V vs Na is worth mentioning. As the scan rate increases, the peaks

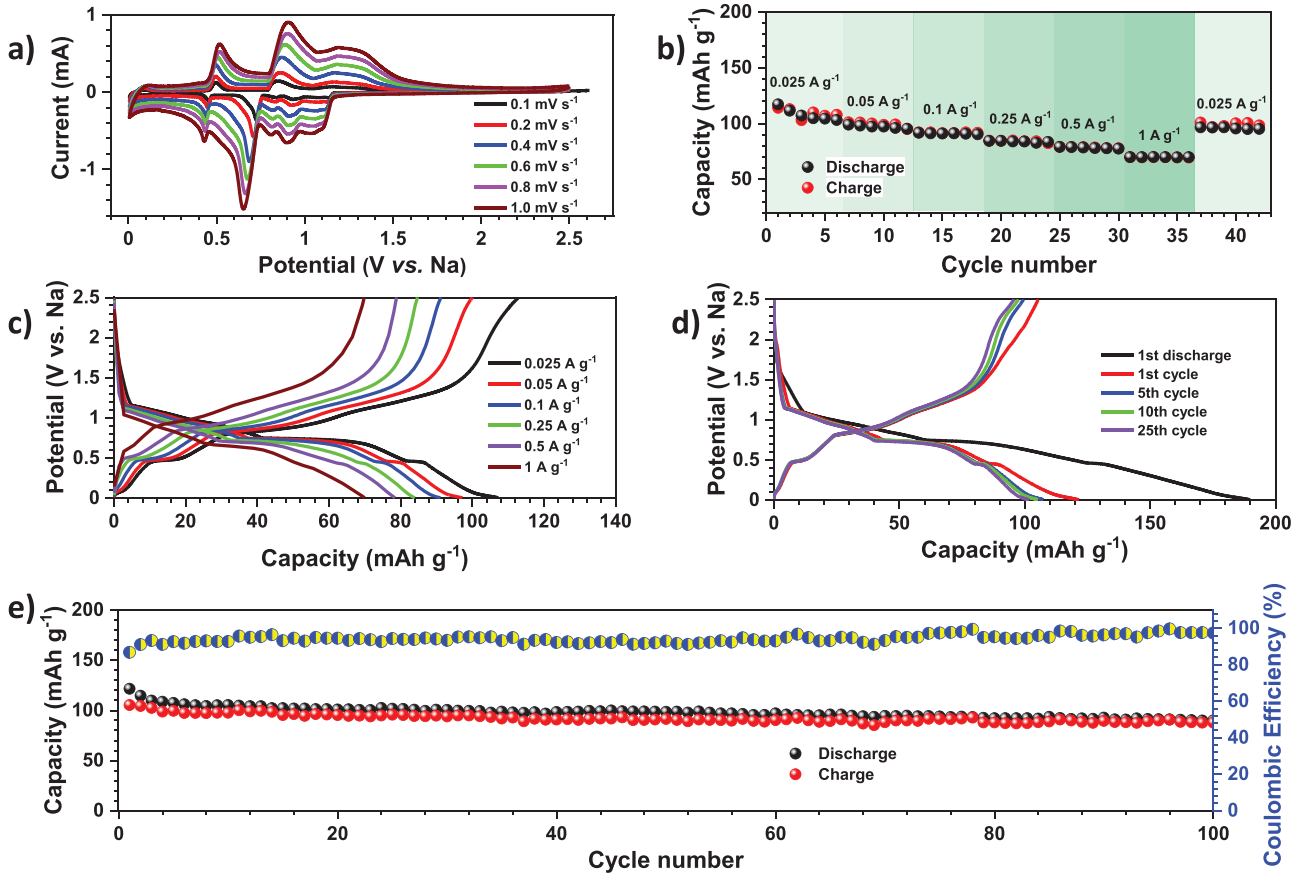

Figure 2. Half-cell performance of RG: a) cyclic voltammetry (CV), b) rate performance, c) charge–discharge curves for rate performance, d) charge–discharge curves at a current density of 50 mA g^{-1}, and e) cycling profile of RG half-cells between 0.005 and 2.50 V versus Na along with Coulombic efficiency at a current density of 50 mA g^{-1}.

start shifting toward a higher potential, along with which the broad peak is seen to become prominent, even merging with the peak at 0.83 V vs Na. No significant change or disappearance of peaks is observed after the first cycle. Nevertheless, an apparent broadening and increase in current are observed for the first scan, which is not observed in the subsequent cycles (Figure S3, Supporting Information). This might be due to the significant volume expansion (70%–100% in electrode level) and associated structural variation/re-arrangement in graphite.[19] It can also arise from an electrolyte decomposition on the electrode surface. The disappearance of the features present in the first cycle points out that volume expansion and electrolyte decomposition are limited to the first cycle. Regardless of the considerable volume expansion, the graphite still retains the cycling stability for many cycles. Goktas et al.[19] studied this phenomenon and concluded that though there is a significant volume variation, it does not entirely ruin the graphitic structure but rather exfoliates it, leaving behind crystalline platelets. The performance of RG in half-cell with increasing current rates were studied (Figure 2b), which displayed promising results. The half-cell maintained 70% of the capacity displayed at a current density of 25 mA g^{-1} even at a high current rate of 1000 mA g^{-1}. When tested at 25 mA g^{-1} after the high current, it reverted to the initial capacity displaying excellent structural stability. The galvanostatic charge–discharge (GCD) curves for the rate performance (Figure 2c) agree with the results visible in the CV curves. A small plateau is visible at ≈0.5 V vs Na at a low rate, which eventually disappears beyond 250 mA g^{-1}. A similar trend is observed in the cathodic scan, where the peak at ≈0.5 V vs Na merges with the peak observed at 0.83 V vs Na, forming a broad peak. A small plateau is visible at ≈0.9 V vs Na in the charge curve, which eventually becomes a part of the sloping curve at higher current rates. This is identical to the rise of a broad peak, which merges with the peak at 0.83 V vs Na. A cycling profile at 50 mA g^{-1} (Figure 2d,e) shows extreme robustness of the RG half-cell, which exhibited a capacity of 87 mAh g^{-1} after 100 cycles at 50 mA g^{-1}. The first discharge shows a lower Coulombic efficiency, crossing 90% in the second cycle. This arises from the volume expansion and electrolyte decomposition detected in the first CV curve. An in situ electrochemical impedance spectroscopic (EIS) study was performed for the RG half-cell for the first, second, tenth, fiftieth, and hundredth cycles from 100 kHz to 10 mHz (Figure S4, Supporting Information). All the other features remain consistent throughout the cycling, establishing the sturdiness of the electrode and its capability to withstand a large number of charge–discharges without any consistent loss of capacity.

2.2. Full-Cell Performance

A full-cell was assembled with RG and in-lab synthesized NVPC cathode, tested in the voltage range 3.1–1.4 V vs Na in glyme family electrolyte. The structural characterization of NVPC was performed to ensure proper phase and composition. The XRD peaks of NVPC (Figure S6a, Supporting Information) match the reported literature without any additional peaks, revealing the absence of any impurities or other phases. The elements present and their respective oxidation phases were analyzed through high-resolution XPS analysis (Figure S6b–f, Supporting Information), which reveals the presence of C, O, P, V, and Na. The presence of carbon was further analyzed through Raman spectroscopy (Figure S6g, Supporting Information), and the carbon content was quantified through a thermogravimetric analysis (TGA) (Figure S6h, Supporting Information), which was around 5 wt%. The morphology and internal structure of NVPC were analyzed with the help of FESEM and HRTEM, which revealed agglomerates of NVPC particles with a highly crystalline nature (Figure S7a,b, Supporting Information). The elemental analysis confirmed the presence of Na, V, P, O, and C, which were detected in the XPS analysis. Further, the distribution of these elements confirmed the homogeneity of NVPC with a uniform carbon coating on their surface (Figure S8a–e, Supporting Information). Before assembling into a full-cell, the electrochemical performance of the cathode was examined in a Na/NVPC half-cell. During CV studies, in the anodic and cathodic scan, we can see a peak positioned at ≈3.5 and ≈3.3 V vs Na, respectively, when studied at a scan rate of 0.1 mV s^{-1} in the voltage range 3.8–2.5 V (Figure S9b, Supporting Information). These correspond to V^{3+} to V^{4+} (3.5 V vs Na) and V^{4+} to V^{3+} (3.3 V vs Na) redox transitions. The charge–discharge curves of NVPC (Figure S9d, Supporting Information) show a single plateau for charge and discharge, affirming that Na-ion storage occurs through the oxidation-reduction of the $V^{3+/4+}$ couple. The cathode material exhibits an excellent rate performance, where it manages to retain its original capacity at 50 mA g^{-1} even after cycling it at a high rate of 1500 mA g^{-1} (Figure S9c, Supporting Information). The cycling stability was also evaluated at a current density of 100 mA g^{-1}, and the cell maintained 87% (79 mAh g^{-1}) after 60 cycles (Figure S9e, Supporting Information).

The RG electrodes were precycled for five cycles before assembling them into a balanced full-cell with NVPC. The RG/NVPC full-cells were cycled between 1.4 and 3.1 V. The anodic scan at a low scan rate of 0.1 mV s^{-1} reveals two peaks at 2.24 and 2.35 V, merged to form one broad peak (**Figure 3**a). They become almost indistinguishable at higher scan rates, and

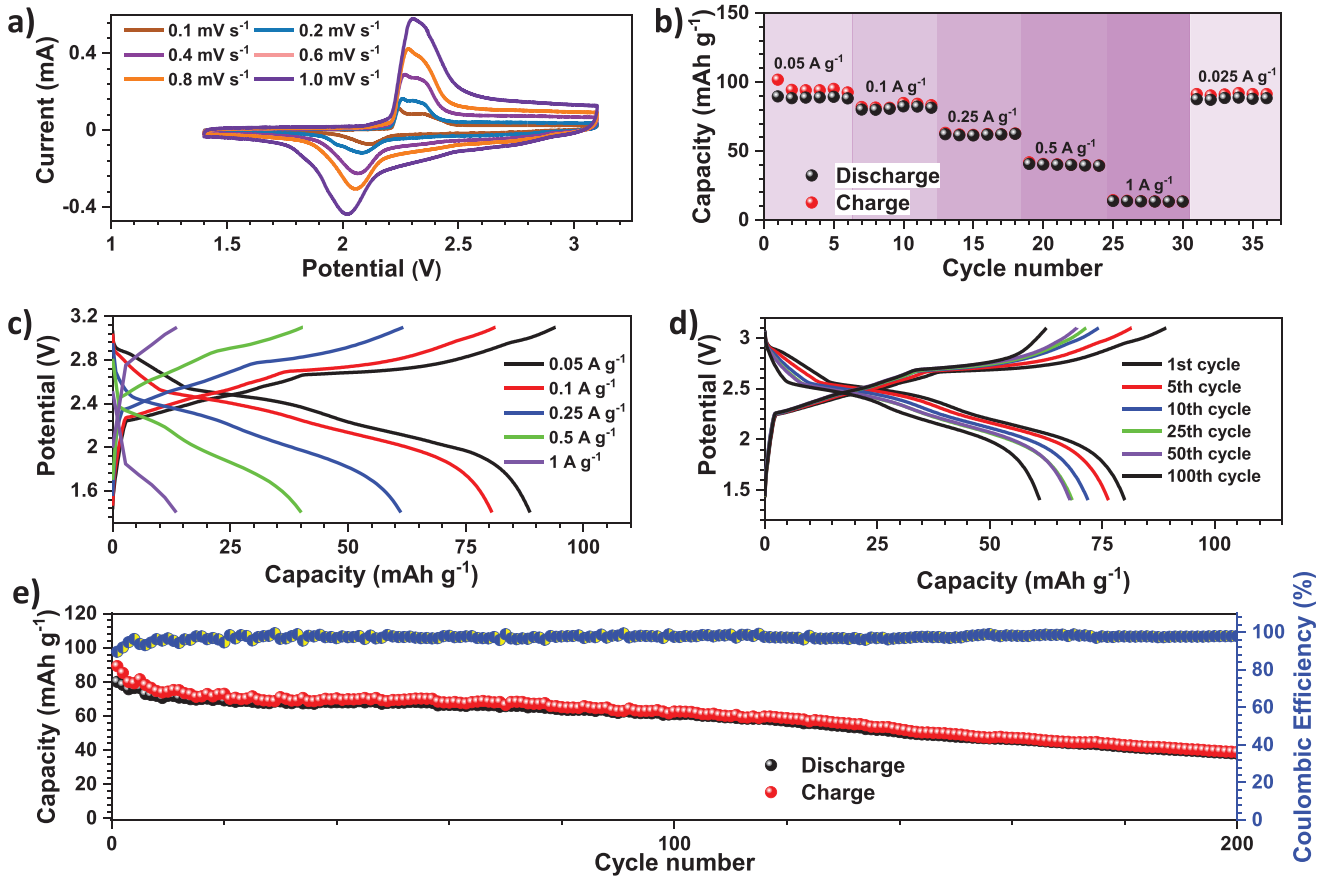

Figure 3. RG/NVPC full-cell performance: a) cyclic voltammetry (CV), b) rate performance, c) charge–discharge curves for rate performance at various current densities, d) charge–discharge curves at a current density of 50 mA g^{-1} between 1.40 and 3.10 V, and e) long-term cycling profile with Coulombic efficiency.

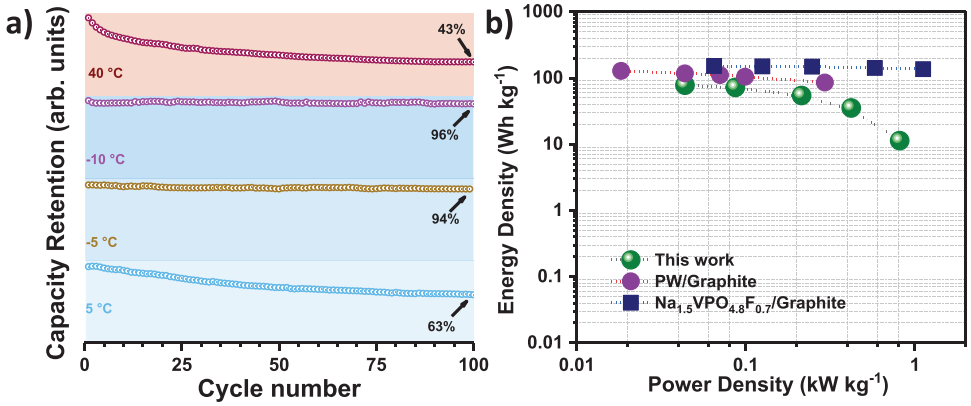

Figure 4. a) Cycling the same RG/NVPC full-cell at 100 mA g^{-1} for 100 cycles between 1.40 and 3.10 V at temperatures of 5, −5, −10, and 40 °C in that order, and b) Ragone plot for RG/NVPC full-cell based on the total active material mass of anode and cathode. Ragone plots of Prussian white/commercial graphite[22] and $Na_{1.5}VPO_{4.8}F_{0.7}$/commercial graphite[11] are also compared.

these individual peaks emerge from the electrochemical reactions at the anode. On the contrary, only one peak is visible in the cathodic scan centered at 2.1 V. This trait continues into higher scan rates. Unfortunately, the full-cell could not maintain a high capacity at current rates of 1000 mA g^{-1}, even though the RG half-cell displayed prominent capacity. We assume this is due to the poor-rate performance of the NVPC cathode. This imbalance in the power density between the electrode active materials might be the contributing factor to such a result seen in the full-cell. Regardless, the cell retains its initial capacity when the current rate switches to a lower value, succeeded by a high current (Figure 3b). This shows that the electrodes can handle the high current without any structural damage that might have caused a reduction in their sodium storage abilities. The charge–discharge curves for the rate performance are shown in Figure 3c. The full-cell was cycled at 50 mA g^{-1} for 200 cycles (Figure 3d,e), where the cell had a discharge capacity of 39 mAh g^{-1}.

Additionally, at different temperatures, a full-cell was cycled 100 times at a current density of 100 mA g^{-1}, shown in **Figure 4**a. This was to study how the capacity retention of the cell is affected by temperature change. Additionally, any long-term effect imparted on the cell due to the temperature difference is also checked. The cell was cycled at temperatures of 5, −5, −10, and 40 °C to simulate low to high-temperature variations, and it retained 63%, 94%, 96%, and 43% of its initial capacity, respectively. The cell displays excellent low-temperature performance, whereas the high-temperature performance is moderate. Due to their physical properties, the electrolyte will not freeze even at such temperatures, making the cell an excellent candidate to operate at subzero temperature conditions. A Ragone plot for the full-cell was also constructed with specific energy and power density at different current rates as shown in Figure 4b. The cell exhibited an energy density of 78 Wh kg^{-1} and a power density of 813 W kg^{-1}, calculated based on the mass of active material in the anode and cathode. In this work, we have explored the half and full-cell performances with one type of salt and solvent for the electrolyte. A comparative study of electrolytes with varying constituents and concentrations can assist in optimizing the performance of the cell. In addition, a cathode with a higher voltage will improve the energy density of the full-cell. Pairing with a cathode with morphology tuned for higher rate performance might also improve the rate performance of the full-cell.[20,21]

3. Conclusion

Graphite was recovered from spent LIBs through a simple, scalable technique and was used as an anode for Na-ion cells through a co-intercalation mechanism. RG half-cell displayed excellent rate performance even at 1000 mA g^{-1}, with a capacity retention of 84% after 100 cycles at a current density of 50 mA g^{-1}. The electrochemical performance of RG proves that the recovery method is facile, novel, and preserves the structure of graphite without losing its Na-storage properties. By pairing with a high-voltage cathode like NVPC, the RG/NVPC full-cell exhibited extremely stable cycling (78% of initial capacity after 100 cycles) and good rate performance. A capacity retention study was performed on a full-cell by varying the temperature of the cell environment, which yielded exemplary low-temperature performance. The cell managed to exhibit good specific energy and power density. RG-based Na-ion cells are cheap, mitigate pollution caused by spent LIBs, and exhibit excellent electrochemical performance. Moreover, the scalability will boost the commercialization potential of RG-based SIBs.

4. Electrochemical Characterization

4.1. RG and NVPC Electrodes

RG electrodes were fabricated by coating a slurry of RG, conductive additive (acetylene black), and polyvinylidene fluoride binder (PVDF) prepared in 1-methyl-2-pyrrolidinone (NMP, anhydrous, Sigma Aldrich, >99.5%) solvent in a ratio of 80:10:10 (wt%), respectively. PVDF was initially dissolved in NMP, followed by the addition of conductive additive and RG, which was stirred overnight at room temperature to ensure homogeneity. Doctor blade technique was used to cast onto Cu foil, which was transferred to an oven at 65 °C until NMP completely evaporated. Using a calendar roller machine, the coated material

on the Cu current collector was pressed. Then, using an electrode cutter, circular electrodes of 12 mm diameters (areal mass loading of active material being 2.12 mg cm^{-2}) were punched. These electrodes were used for the half-cell studies.

NVPC electrodes were fabricated through a manual process. A freestanding film was initially made with NVPC, acetylene black, and binder (teflonized acetylene black, TAB-2) with ethanol as a solvent in a ratio of 4:2:1 (wt%) in an agate mortar pestle. This was pressed onto a stainless steel mesh (Goodfellow, UK) of diameter 14 mm with a Specac hydraulic press in a pellet maker (areal mass loading of active material being ≈2.6 mg cm^{-2}). For the full-cell studies, NVPC electrodes were made similarly with active material mass adjusted to balance the capacity of the anode during precycling.

4.2. Half-Cell and Full-Cell Studies

Both half- and full-cells have been fabricated in an inert glove box workstation (MBraun, Germany, O_2 < 0.1 ppm and H_2O < 0.1 ppm) in a CR2016 coin cell using a glass microfiber separator (Whatmann, cat no. 1825-047, UK). Half-cell fabrication of both RG and NVPC was done to obtain their electrochemical performance with sodium metal as the reference and counter electrode. Before RG half-cell fabrication, the electrodes were kept at 75 °C in a vacuum oven for at least 4 h, whereas the NVPC was kept at 75 °C in a vacuum oven for at least 24 h to ensure complete moisture removal. 1 M $NaCF_3SO_3$ (98%, Sigma Aldrich) in tetraethylene glycol dimethyl ether (TEGDME, >99%, Sigma Aldrich) was prepared first, and molecular sieves were added to the electrolyte to remove any moisture and left for 24 h before usage. This electrolyte was used in all electrochemical studies. Before full-cell fabrication, RG was precycled five times, followed by which it was carefully decrimped inside the glove box and assembled into a full-cell. The anode and cathode in full-cell were assembled with stainless steel mesh as the current collector and TAB as the binder. The anode areal mass loading of active material for the full-cell is ≈6.5 mg cm^{-2}. BioLogic battery tester (BCS-805) was used to perform electrochemical tests for half- and full-cells, and Espec SU-242 benchtop type thermal chamber was used to control the temperature to evaluate the temperature-dependent performance of the cell.

5. Material Characterization

Rigaku Smartlab automated multipurpose X-ray diffractometer with a monochromatic Cu Kα radiation (λ = 1.5604 Å) was used to study the crystallographic parameters of RG and NVPC with a scan rate of 0.5° min^{-1} to obtain high-resolution peaks. The surface composition and oxidation states were analyzed through high-resolution XPS (Multilab, 2000, UK). Raman spectroscopy of RG was performed to analyze the orderliness of the sample, using a 515 nm diode laser as a light source at room temperature (LabRam HR800 UV Raman microscope, Horiba Jobin-Yvon, France). The sample's surface imaging and elemental composition were evaluated through FESEM (S-4700, Hitachi, Japan) and HRTEM (JEM-2000, EX-II, JEOL, Japan). TGA (Shimadzu, Japan) was performed at 5 °C min^{-1} in an air atmosphere.

6. Experimental Section

Recovery of Graphite from Spent LIBs: Graphite was recovered from spent LIB through a reported procedure[23] followed by additional calcination (**Scheme 1**). The spent LIBs were immersed in NaCl solution overnight, with the anode and cathode leads in water. The battery voltage was measured with a multimeter to ensure the complete discharge. The above process was repeated until the voltage was ≈0 V. The battery was opened, and the anode (graphite coated on Cu foil) was kept aside. Graphite was carefully scratched off from the copper foil. The obtained graphite was transferred to a beaker in which enough N, N-dimethylformamide (DMF, anhydrous, 99.8%, Sigma Aldrich) was added to immerse the graphite. The beaker was placed in a silicon oil bath at 90 °C and was subjected to stirring for 24 h. This is to ensure the complete dissolution of the binder. After 24 h, the suspension was allowed to settle, followed by which DMF was decanted carefully with minimum to no loss of graphite. The obtained graphite was heated at 150 °C for 12 h in the air to remove any DMF presence. This was cooled to room temperature and ground well using an agate mortar pestle, followed by heating at 700 °C for 2 h (heating ramp rate of 5 °C min^{-1}) under argon atmosphere to obtain the RG that was used as active material.

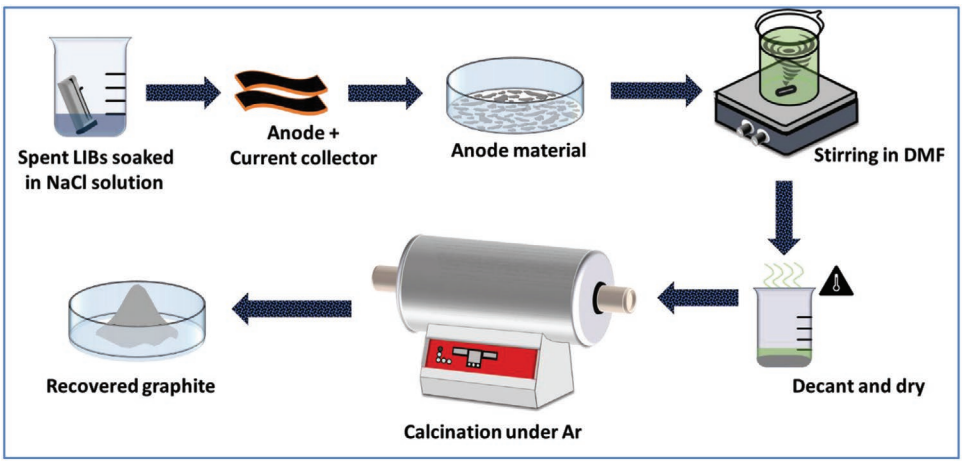

Scheme 1. Schematic illustration of recovery of graphite from spent LIBs.

Synthesis of Carbon-Coated $Na_3V_2(PO_4)_3$ (NVPC): The cathode, NVPC, was synthesized by adapting the method from a previously reported work through ball milling followed by pyrolysis.[24] A mixture of NaH_2PO_4. H_2O (Extra Pure, HIMEDIA), NH_4VO_3 (>99%, Sigma Aldrich), and citric acid (>99.5%, Sigma Aldrich) in a 3:2:3 molar ratio was ball-milled with ethanol for 24 h at 300 rpm in a Retsch PM 200 planetary ball miller with a 6:1 ball to material mass ratio. The mixture obtained was dried at 70 °C overnight, ground in an agate mortar pestle, pyrolyzed at 800 °C for 8 h with a heating ramp rate of 5 °C min^{-1}, and cooled to room temperature under natural cooling.

Supporting Information

Supporting Information is available from the Wiley Online Library or from the author.

Acknowledgements

K.S. thanks the Department of Science and Technology (DST), Government of India, for the financial support through INSPIRE fellowship (IF180157). Y.-S.L. acknowledges the financial support from the National Research Foundation of Korea (NRF) grant funded by the Korean government (Ministry of Science, ICT & Future Planning) (No. 2019R1A2C1007620). V.A. acknowledges the financial support from the Science and Engineering Research Board (SERB), a statutory body of DST, through Swarnajayanti Fellowship (SB/SJF/2020-21/12).

Conflict of Interest

The authors declare no conflict of interest.

Data Availability Statement

The data that support the findings of this study are available from the corresponding author upon reasonable request.

Keywords

graphite anode, Li-ion battery recycling, $Na_3V_2(PO_4)_3$ cathode, Na-ion battery

Received: March 17, 2022
Revised: April 21, 2022
Published online: May 15, 2022

[1] M. E. H. Assad, A. Khosravi, M. Malekan, M. A. Rosen, M. A. Nazari, *Design and Performance Optimization of Renewable Energy Systems* (Eds: M. E. H. Assad, M. A. Rosen), Academic, San Diego, CA **2021**, pp. 205–219.
[2] K. Subramanyan, M. L. Divya, V. Aravindan, *J. Mater. Chem. A* **2021**, 9431.
[3] K. Subramanyan, V. Aravindan, *Chem* **2019**, *5*, 3096.
[4] S. Natarajan, K. Subramanyan, V. Aravindan, *Small* **2019**, *15*, 1904484.
[5] K. Subramanyan, Y.-S. Lee, V. Aravindan, *J. Colloid Interface Sci.* **2021**, *582*, 51.
[6] H. Moriwake, A. Kuwabara, C. A. J. Fisher, Y. Ikuhara, *RSC Adv.* **2017**, *7*, 36550.
[7] B. Jache, P. Adelhelm, *Angew. Chem., Int. Ed. Engl.* **2014**, *53*, 10169.
[8] G. Yoon, H. Kim, I. Park, K. Kang, *Adv. Energy Mater.* **2017**, *7*, 1601519.
[9] H. Kim, J. Hong, G. Yoon, H. Kim, K.-Y. Park, M.-S. Park, W.-S. Yoon, K. Kang, *Energy Environ. Sci.* **2015**, *8*, 2963.
[10] H. Kim, J. Hong, Y.-U. Park, J. Kim, I. Hwang, K. Kang, *Adv. Funct. Mater.* **2015**, *25*, 534.
[11] Z.-L. Xu, G. Yoon, K.-Y. Park, H. Park, O. Tamwattana, S. K. Joo, W. M. Seong, K. Kang, *Nat. Commun.* **2019**, *10*, 2598.
[12] J. Park, Z.-L. Xu, K. Kang, *Front. Chem.* **2020**, *8*, 432.
[13] K. Subramanyan, S. Natarajan, Y. S. Lee, V. Aravindan, *Chem. Eng. J.* **2020**, *397*, 125472.
[14] M. L. Divya, S. Natarajan, Y.-S. Lee, V. Aravindan, *J. Mater. Chem. A* **2020**, *8*, 4950.
[15] M. L. Divya, Y.-S. Lee, V. Aravindan, *Batteries Supercaps* **2021**, *4*, 671.
[16] M. L. Divya, S. Natarajan, Y.-S. Lee, V. Aravindan, *ChemSusChem* **2020**, *13*, 5654.
[17] K. Liu, S. Yang, L. Luo, Q. Pan, P. Zhang, Y. Huang, F. Zheng, H. Wang, Q. Li, *Electrochim. Acta* **2020**, *356*, 136856.
[18] R. I. R. Blyth, H. Buqa, F. P. Netzer, M. G. Ramsey, J. O. Besenhard, P. Golob, M. Winter, *Appl. Surf. Sci.* **2000**, *167*, 99.
[19] M. Goktas, C. Bolli, E. J. Berg, P. Novák, K. Pollok, F. Langenhorst, M. V. Roeder, O. Lenchuk, D. Mollenhauer, P. Adelhelm, *Adv. Energy Mater.* **2018**, *8*, 1702724.
[20] J. Xu, E. Gu, Z. Zhang, Z. Xu, Y. Xu, Y. Du, X. Zhu, X. Zhou, *J. Colloid Interface Sci.* **2020**, *567*, 84.
[21] E. Gu, J. Xu, Y. Du, X. Ge, X. Zhu, J. Bao, X. Zhou, *J. Alloys Compd.* **2019**, *788*, 240.
[22] S. G. Patnaik, I. Escher, G. A. Ferrero, P. Adelhelm, *Batteries Supercaps* **2022**, e202200043.
[23] S. Natarajan, D. S. Lakshmi, H. C. Bajaj, D. N. Srivastava, *J. Environ. Chem. Eng.* **2015**, *3*, 2538.
[24] R. Klee, M. J. Aragón, R. Alcántara, J. L. Tirado, P. Lavela, *Eur. J. Inorg. Chem.* **2016**, *2016*, 3212.